Performance and adsorption mechanism of a magnetic calcium silicate hydrate composite for phosphate removal and recovery

Lihong Peng, Hongliang Dai, Yifeng Wu, Zheqin Dai, Xiang Li and Xiwu Lu

ABSTRACT

A novel magnetic calcium silicate hydrate composite (Fe_3O_4@CSH) was proposed for phosphorus (P) removal and recovery from a synthetic phosphate solution, facilitated by a magnetic separation technique. The Fe_3O_4@CSH material was characterized by transmission electron microscopy (TEM), scanning electron microscopy (SEM), powder Fourier transform infrared (FTIR) spectroscopy, X-ray diffraction (XRD), X-ray photoelectron spectroscopy (XPS), zeta-potential and magnetic curves. The chemical composition and structure of Fe_3O_4@CSH and the successful surface loading of hydroxyl functional groups were confirmed. Phosphate adsorption kinetics, isotherm, and thermodynamic experiments showed that adsorption reaches equilibrium at 24 h, with a maximum adsorption capacity of 55.84 mg P/g under optimized experimental conditions. Adsorption kinetics fitted well to the pseudo second-order model, and equilibrium data fit the Freundlich isotherm model. Thermodynamic analysis provided a positive value for ΔH° (129.84 KJ/mol) and confirmed that phosphate adsorption on these materials is endothermic. The P-laden Fe_3O_4@CSH materials could be rapidly separated from aqueous solution by a magnetic separation technique within 1 min. A removal rate of more than 60% was still obtained after eight adsorption/desorption cycles, demonstrating the excellent reusability of the particles. The results demonstrated that the Fe_3O_4@CSH materials had high P-adsorption efficiency and were reusable.

Key words | adsorption, calcium silicate hydrate, magnetic nanoparticles, magnetic separation, phosphorus recovery

Lihong Peng†
Hongliang Dai†
Yifeng Wu
Zheqin Dai
Xiang Li
Xiwu Lu (corresponding author)
School of Energy and Environment,
Southeast University,
No. 2 Sipailou Road, Nanjing 210096,
China
E-mail: *xiwulu@seu.edu.cn*;
xiwuluseu1@163.com

Lihong Peng†
Hongliang Dai†
Zheqin Dai
Xiang Li
Xiwu Lu
ERC Taihu Lake Water Environment (Wuxi),
No. 99 Linghu Road, Wuxi 214135,
China

Hongliang Dai†
School of Environmental and Chemical Engineering,
Jiangsu University of Science and Technology,
Zhenjiang 212018,
China

†These authors contributed equally to this work and should be considered co-first authors.

INTRODUCTION

Phosphorus (P) is a non-renewable resource and a non-substitutable component of all living organisms, and it also plays a prominent role in eutrophication of water bodies (Cordell *et al.* 2009; Mayer *et al.* 2016). Excess P can be discharged into the aquatic environment through agricultural runoff and sewage discharge, and currently, most P used in industry and agriculture is obtained from natural phosphate rock deposits, which are being progressively depleted on a global scale (Correll 1998; Gilbert 2009). Eutrophication and excessive natural resource consumption are some of the most formidable challenges facing global society, and it is therefore essential to control P emissions and achieve P recovery.

To date, various physicochemical approaches have been developed and applied to recover P from wastewater, including chemical precipitation, crystallization, filtration, membranes, electrochemical techniques, biological uptake, adsorption, and anion exchange (Jordaan *et al.* 2010; Renman & Renman 2010; Loganathan *et al.* 2014; Egle *et al.* 2015; Luo *et al.* 2015; Almatouq & Babatunde 2016; Tarayre *et al.* 2016). Of these, crystallization and adsorption are considered the most promising options due to their simple design, ease of operation, high efficiency, and low environmental risk (Loganathan *et al.* 2014; Egle *et al.* 2015; Dai *et al.* 2016, 2017). Calcium silicate hydrate (CSH) has been extensively investigated for crystallization due to its extremely slow Ca^{2+} release, alkalinity supply capacity, unique morphology, and good adsorption properties (Guan *et al.* 2013; Okano *et al.* 2013). In a seeded crystallization process, suitable seed materials with an isomorphic

doi: 10.2166/wst.2018.184

crystal plane initiate and promote the deposition of calcium phosphate (Ca-P) onto the surface of seeds at a low saturation index, mainly by eliminating the energy barrier (Song *et al.* 2006). CSH is a hydration product of physical and chemical binding between siliceous and calcareous substrates, and it usually coexists with other crystal phases such as calcium hydroxide ($Ca(OH)_2$) and unreacted phases (Li *et al.* 2017). Previous studies have demonstrated that the effectiveness of CSH materials is dependent on synthetic conditions, including the silicon material, Ca/Si molar ratios, the hydrothermal reaction temperature and time, and the stirring strength, which consequently influence the chemical components, microscopic morphology, and microstructure of materials (Guan *et al.* 2013; Okano *et al.* 2013). P-laden CSH has been shown to have good reactivity, settleability, filterability, dewatering, and feasibility compared to P precipitated with conventional $CaCl_2$ and $Ca(OH)_2$, and it therefore shows promise for P recovery (Okano *et al.* 2013). One previous study recovered a Ca-P product with a total P content of 18.64%, comparable to natural phosphate rock (Guan *et al.* 2013). Although the CSH system has been investigated for decades, the difficulty in separating fine crystallites after crystallization has limited its practical application to wastewater treatment and P recovery. For practical operation to be economically viable, the recovered P loaded onto CSH particles should settle as quickly as possible, resulting in high recovery efficiency. Thus, a significant challenge in P recovery by crystallization is the exploration of novel, high-performance, quickly separated, and easily recycled seeds to achieve easy, low-cost P recovery from wastewater.

Over the past decades, magnetic nanoparticles (MNPs, particularly magnetite [Fe_3O_4]) have received considerable attention for their unique nano-sized and morphology-dependent physico-chemical properties, and for their biocompatibility, magnetic properties, and strong P-binding affinity and capacity (Daou *et al.* 2007; Drenkova-tuhtan *et al.* 2013; Tang & Lo 2013; Yoon *et al.* 2014). A convenient, compact, and efficient P-recovery system in wastewater treatment could be developed based on these properties. Direct use of 20 nm Fe_3O_4 particles for phosphorus recovery has been investigated previously, and a maximum adsorption capacity of 5.03 mg P/g was reported (Yoon *et al.* 2014). However, due to high surface free energy, Fe_3O_4 MNPs with fewer functional groups are susceptible to air oxidation and leaching under acidic conditions, and prone to aggregation in aqueous solutions, which reduces the P-removal capacity and restricts the range of applications for these materials (Tang & Lo 2013; Zong *et al.* 2013). Furthermore, the adsorption capacity of Fe_3O_4 MNPs is relatively low, and further enhancement is required.

CSH incorporated into Fe_3O_4 MNPs is one system that may enhance the feasibility of P recovery and address the issues discussed through improved efficiency and settleability. In this study, we report a novel synthesis method for magnetic calcium silicate hydrate composite (Fe_3O_4@CSH) materials via dynamic hydrothermal synthesis in an autoclave. Various synthetic conditions were pre-screened to determine the most effective system for phosphate adsorption from a synthetic phosphate solution. The as-prepared materials were characterized by transmission electron microscopy (TEM), scanning electron microscopy (SEM), Fourier transform infrared (FTIR) spectroscopy, powder X-ray diffraction (XRD), X-ray photoelectron spectroscopy (XPS), zeta-potential, and magnetic curves to better understand the adsorption mechanisms of phosphate. In addition, adsorption kinetics and equilibrium isotherm models were used for data analysis, and thermodynamic parameters calculated. Kinetic, equilibrium, and thermodynamic experiments were performed to characterize the phosphate adsorption performance of the magnetic composite materials, and the reusability of the materials was demonstrated over eight adsorption/desorption cycles at the laboratory scale.

MATERIALS AND METHODS

Materials

Ferric chloride hexahydrate ($FeCl_3 \cdot 6H_2O$, ≥99.0%), polyethylene glycol (EG, ≥99.9%), ethanol (EtOH, ≥99.7%), sodium hydroxide (NaOH, ≥99.0%), hydrochloric acid (HCl, 36–38 wt%), and potassium dihydrogen phosphate (KH_2PO_4) were purchased from Sinopharm Chemical Reagent Co., Ltd (Wuxi, China). Sodium acetate anhydrous (NaOAc, ≥99.0%), trisodium citrate dehydrate (Na_3Cit, ≥99.0%), and calcium oxide (CaO, >98%) were purchased from Shanghai Chemical Reagent Co., Ltd (Shanghai, China). White carbon black (mainly SiO_2, spherical particles with a homogeneous 10-μm diameter) was purchased from Shanghai Macklin Biochemical Co., Ltd (Shanghai, China). All chemicals were of analytical grade and were used without further purification.

Synthesis of Fe_3O_4@CSH materials

The synthesis of Fe_3O_4 MNPs was conducted using a solvothermal method based on previous studies (Song *et al.* 2014;

Wang et al. 2016). $FeCl_3 \cdot 6H_2O$ (4.05 g), NaOAc (4.0 g), and Na_3Cit (2.16 g) were dissolved in EG (120 mL). Then, the mixture was stirred vigorously for 40 min, sealed in a Teflon-lined stainless-steel autoclave (heating power = 0.8 kw), and heated at 200 °C for 8 h. After cooling to room temperature, the resulting Fe_3O_4 MNPs were washed several times with ultra-pure water and ethanol, and then dried under vacuum at 70 °C for 8 h prior to further use.

The novel Fe_3O_4@CSH materials were synthesized from the as-synthesized Fe_3O_4 MNPs, CaO, and SiO_2 using a dynamic hydrothermal synthesis method. The optimized Fe_3O_4@CSH formulation was as follows: as-prepared Fe_3O_4 (1 g), white carbon black (1.29 g), and CaO (2.66 g) dissolved in 150 mL of ultra-pure water, and homogenized by ultrasonication for 15 min at room temperature. This homogeneous mixture was poured into an autoclave and hydrothermally reacted at 170 °C for 7 h, with stirring at 90 rpm. The resulting products were removed after the temperature and pressure were reduced to atmospheric conditions. The as-prepared particles were washed thoroughly several times with ultra-pure water to remove any excess ions, and the washed precipitates were then dried at 70 °C overnight and finely pulverized for phosphate adsorption.

Characterization of materials

The morphology of the as-prepared materials was determined using SEM (Hitachi S4800, Japan) and TEM (JEOL JEM-1200EX, Japan) at an accelerating voltage of 120 kV. FTIR spectra were recorded at a resolution of 4 cm^{-1} in the range 400–4,000 cm^{-1} using a spectrometer (FTIR, Nicolet 6700, USA) with KBr pellets at room temperature. XRD analysis was conducted on a diffractometer (XRD, Bruker D8 Advance, Germany) using a Cu Kα source (λ = 1.5406 Å). The Brunauer–Emmett–Teller (BET) surface area and micropore area were measured using a surface area analyzer (ASAP-2460e, Micromeritics, USA) through the nitrogen adsorption experiment. A zeta potential analyzer (Zetasizer Nano ZS, Malvern, UK) was used at room temperature for zeta potential measurements. XPS experiments were conducted using an ESCALAB 250XI system multi-detection analyzer (Thermo Fisher Scientific, USA) fitted with monochromatized Al and Ka (ha = 1,486.6 eV) X-ray sources at a residual pressure of 10^{-8} Pa. All binding energies were referenced to the C1s peak at 284.5 eV. Magnetic measurements were carried out in a vibrating sample magnetometer (VSM, Versalab, USA) in the magnetic field range of −30 to 30 kOe, and the saturated magnetization of the materials was measured through the plotted magnetization curves.

Adsorption experiments

Phosphate adsorption experiments on the as-prepared materials were performed by a batch adsorption technique at 25 ± 1 °C. For kinetic studies, several 100-mL phosphate solutions of known initial concentration (20 mg P/L) were placed into 250-mL conical flasks with a fixed adsorbent dosage (0.6 g/L) for a range of reaction times (0.08 and 24 h) at a range of temperatures (25 °C, 35 °C, 45 °C). Adsorption isotherm experiments were conducted by suspending 0.06 g of the adsorbents in 100-mL phosphate solutions with initial P concentrations ranging from 20 to 55 mg P/L at room temperature. The solutions were maintained at an initial pH (about 5.35) without artificial pH adjustment unless otherwise stated, and shaken at a speed of 150 rpm using a reciprocating thermostatic shaker for both adsorption kinetics and isotherm experiments. The cyclic experiments were performed with eight adsorption/desorption cycles of Fe_3O_4@CSH to test the reusability of the particles. The phosphate desorption experiments were conducted by suspending P-loaded Fe_3O_4@CSH particles in a desorption solution (1 M HCl) with an adsorption-to-desorption volume ratio of 10:1 for 24 h. Thereafter, the recycled particles were reused for the next cycle of the phosphate adsorption experiment. For all adsorption experiments, phosphate removal from synthetic phosphate solutions was facilitated by rapid magnetic separation using an external magnetic field. After magnetic separation, the P concentrations in supernatants were analyzed by the molybdenum blue colorimetric method (Murphy-Riley method) (Murphy & Riley 1962) with absorbance measured using UV 9100 B UV-vis spectrophotometer at a wavelength of 700 nm corresponding to the maximum absorption of phosphate. The amount of adsorbed phosphate was calculated by the difference between initial and final P concentrations in solution using the following Equation (1).

$$q_e = \frac{(C_0 - C_t) \cdot V}{W} \quad (1)$$

where, q_e is the phosphate adsorbed at equilibrium, C_0 is the initial P concentration in solution (mg P/L) and C_t is the P concentration (mg P/L) in any time; V is the volume of solution (L) and W is the dry mass of adsorbents (g).

The P removal efficiency (η) was calculated through the following Equation (2).

$$\eta = \frac{(C_0 - C_e)}{C_0} \times 100 \quad (2)$$

where C_0 is the initial P concentration in solution (mg P/L) and C_e is the P concentration at equilibrium (mg P/L). Each batch experiment was performed in triplicate, and the mean data as well as experimental errors were reported.

Adsorption models

Utilization of the appropriate chemical model can provide useful information for further understanding the underlying adsorption mechanisms. From the perspective of view, three kinetic adsorption models, the pseudo first-order (Equation (3)), pseudo second-order (Equation (4)) and Elovich (Equation (5)) kinetic models (Sen & Bhattacharyya 2011), were employed to fit and analyze the kinetic experimental data.

$$q_t = q_e\left(1 - e^{-k_1 t}\right) \quad (3)$$

$$q_t = \frac{k_2 q_e^2 t}{1 + k_2 q_e t} \quad (4)$$

$$q_t = \frac{1}{\beta}\mathrm{In}(\alpha\beta) + \frac{1}{\beta}\mathrm{In}(t) \quad (5)$$

where q_e and q_t are the phosphate adsorbed (mg P/g) at equilibrium time (h) at time t (h), respectively; k_1 and k_2 were the kinetic rate constants of the pseudo first-order and pseudo second-order kinetic models (h^{-1}), respectively; α and β represent the initial adsorption rate constant (mg P g^{-1} h^{-1}) and the Elovich adsorption constant (g mg P^{-1}), respectively.

In order to further understand the phosphate adsorption mechanism and evaluate the efficiency of Fe_3O_4@CSH materials, adsorption equilibrium was established and depicted by a plot of the adsorbed P and the residual P (C_e-q_e) in the solution. Wherein, initial P concentration as a variable parameter was designed to investigate the isotherms of phosphate adsorption onto these particles in sufficient time (24 h). Three typical isotherm models (Freundlich (Equation (6)), Langmuir (Equation (7)), and Redlich-Peterson (Equation (8)) isotherm models) (Foo & Hameed 2010), were adopted to fit and analyze the data of adsorption isotherm experiments.

$$q_e = K_F C_e^{1/n} \quad (6)$$

$$q_e = \frac{Q_{max} K_L}{1 + C_e} \quad (7)$$

$$q_e = \frac{K_R C_e}{1 + a_R C_e^g} \quad (8)$$

where q_e is the phosphate adsorbed in the adsorbents; C_e is the P concentration (mg P/L) at equilibrium; K_F, K_L and K_R are the Freundlich isotherm constant (L/g) related to adsorption capacity, the Langmuir isotherm constant (L P mg^{-1}) and the Redlich-Peterson isotherm constant (L/g), respectively; 1/n is the Freundlich isotherm constant (dimensionless) related to the adsorption capacity; Q_{max} is the maximum P adsorption capacity (mg P/g); a_R and g are the Redlich-Peterson constant related to the affinity of the binding sites (L P mg^{-1}) and the Redlich-Peterson isotherm exponent (dimensionless) related to the adsorption intensity, respectively.

Further, a thermodynamic model was proposed to study the effect of temperature on P adsorption and subsequently determine the phosphate-adsorption mechanism. The thermodynamic experiment as a function of different temperatures was performed to characterize the adsorption of phosphate onto the surface of Fe_3O_4@CSH materials. Accordingly, the obtained experimental data were employed to conduct thermodynamic analysis by the following equations (Goswami & Purkait 2011).

$$\Delta G^0 = \Delta H^0 - T\Delta S^0 \quad (9)$$

$$\Delta G^0 = -RT\mathrm{In}K^0 \quad (10)$$

$$\mathrm{In}K^0 = \frac{\Delta S^0}{R} - \frac{\Delta H^0}{RT} \quad (11)$$

$$K_0 = \frac{a q_e}{C_e} \quad (12)$$

whereas ΔG^0 is the change in Gibb's free energy, ΔS^0 is the change in entropy, ΔH^0 is the change in enthalpy, R is the universal gas constant 8.314 J/mol/K) and T is the experimental absolute temperature (K); K_e and a are the equilibrium constant (dimensionless) and the adsorbent dosage (g/L) respectively.

To obtain thermodynamic model parameters, a curve of $\ln(K_e)$ versus 1/T was plotted, and fitted with Equation (11). The values of ΔS^0 and ΔH^0 were calculated from the slope and intercept of the plot, and the value of ΔG^0 was calculated using the Van't Hoff Equation (9); K_e was determined by the method described in Lyubchik *et al.* 2004.

RESULTS AND DISCUSSION

Characterization of materials

The morphology, structure and magnetic property characterization results for the synthesized materials are summarized in Figure 1. As shown in Figure 1(a) and 1(c), the as-synthesized Fe_3O_4 was composed of spherical-shaped MNPs with an average diameter of about 200 nm. Figure 1(b) and 1(d) show that the Fe_3O_4@CSH materials were spherical, with an average diameter of about 400 nm. This increase in diameter indicates successful coating of silica and calcium layers. The surface functionalization with CSH could not be seen in the TEM image, perhaps because the modification reaction occurs only on the particle surfaces, and the grafted molecular layer was too thin to be identified using TEM (Zhao *et al.* 2014). The BET surface areas of the particles were measured using micropore analysis; the results showed that the CSH coating led to a slight decline in the Fe_3O_4 surface area from 77.1 to 66.8 m^2/g, perhaps due to the increased particle size and the agglomeration of CSH with Fe_3O_4.

FTIR spectroscopy was conducted to identify changes in surface functional groups on Fe_3O_4@CSH before and after phosphate adsorption; the results are shown in Figure 1(e). The appearance of a peak at 579 cm^{-1} was attributed to the Fe–O stretching vibration (Das *et al.* 2009; Zhao *et al.* 2014). The band at 470 cm^{-1} was due to the O–Si–O bending vibration, the band around 1,080 cm^{-1} corresponds to Si–O–Si stretching vibrations, and the band at 983 cm^{-1} relates to Si–O–H stretching vibration (Das *et al.* 2009; Sadeghi *et al.* 2012). From these results, it can be concluded that the silica layer was coated successfully on the particle surfaces. In addition, the FTIR spectra of Fe_3O_4@CSH after phosphate adsorption show a new broad band around 1,038 cm^{-1} (Figure 1(e)) corresponding to the $H_2PO_4^-$ and HPO_4^{2-} V3 band vibration (Elzinga & Sparks 2007), and implying that $Ca(H_2PO_4)_2$ and $CaHPO_4$ dominated in the adsorbed phosphate. This result corresponds well with other studies, which also found that $Ca(H_2PO_4)_2$ and $CaHPO_4$ were the dominant P-recovered products (Guan *et al.* 2013; Okano *et al.* 2013). The band at approximately 1,642 cm^{-1} relates to the H_2O bending vibration, indicating hydration of SiO_2 and CaO on the Fe_3O_4 surface. Broad OH absorption peaks occurred at 3,400–3,600 cm^{-1} in the Fe_3O_4@CSH material spectrum, possibly caused by the OH stretching vibration peak on the silica or magnetite surface. A large number of OH groups on the particle surface can contribute to the adsorption of phosphate. The structure of the prepared materials and the phosphate removal mechanism was investigated further by XRD; the XRD patterns are shown in Figure 1(f). Figure 1(f) shows that the XRD pattern of the Fe_3O_4@CSH particles has an extra band around $2\theta = 25^\circ$, arising from the presence of the amorphous silica component, in agreement with the FTIR results (Zhang *et al.* 2013). The existence of $Ca(OH)_2$ in the XRD spectrum confirms the successful coverage of the formed $Ca(OH)_2$, in good agreement with the TEM results.

XPS was conducted to characterize the chemical composition and chemical state of the materials obtained; the O 1 s and Fe 2p XPS results for the three materials are shown in Figure 2. The atomic concentrations of each element are summarized in Table 1. The O 1 s XPS spectra could be well fitted with four peaks at 530.2, 530.6, 531.9, and 533.4 eV, indicating Fe–O, Ca–O or composite O, O–Si–OH, and O–C (Fang *et al.* 2017). The O 1 s XPS spectra of Fe_3O_4 and Fe_3O_4@CSH showed an increase in the fraction of O-Si-OH from 45.6% to 57.1%, while the fraction of O-Si-OH decreased sharply to 31.7% after phosphate adsorption (Table 2). This indicates the possibility that strong surface complexation occurred between O-Si-OH and phosphate. As shown in Figure 2, notable differences in the O 1 s XPS spectra were observed before and after phosphate adsorption. A new peak associated with P–O is clearly observed in the O 1 s XPS spectrum of Fe_3O_4@CSH after phosphate adsorption, implying that the phosphate was adsorbed on Fe_3O_4@CSH and complexed with OH-containing functional groups, consistent with the FTIR result. To determine the possible bonding of P with the adsorbent, Fe 2p XPS spectra of Fe_3O_4@CSH before and after phosphate adsorption were measured and analyzed (Figure 2, Table 3). Figure 2 shows six relative peaks to Fe 2p, at 710.1 and 723.7 eV corresponding to Fe_3O_4, and at 712.0, 725.6, 720, and 733.6 eV, respectively, corresponding to FeOOH or containing Fe^{3+} composites. The small variation in FeOOH binding energy after phosphate adsorption could be attributed to a small amount of phosphate adsorption onto Fe_3O_4@CSH complexed with Fe-containing functional groups.

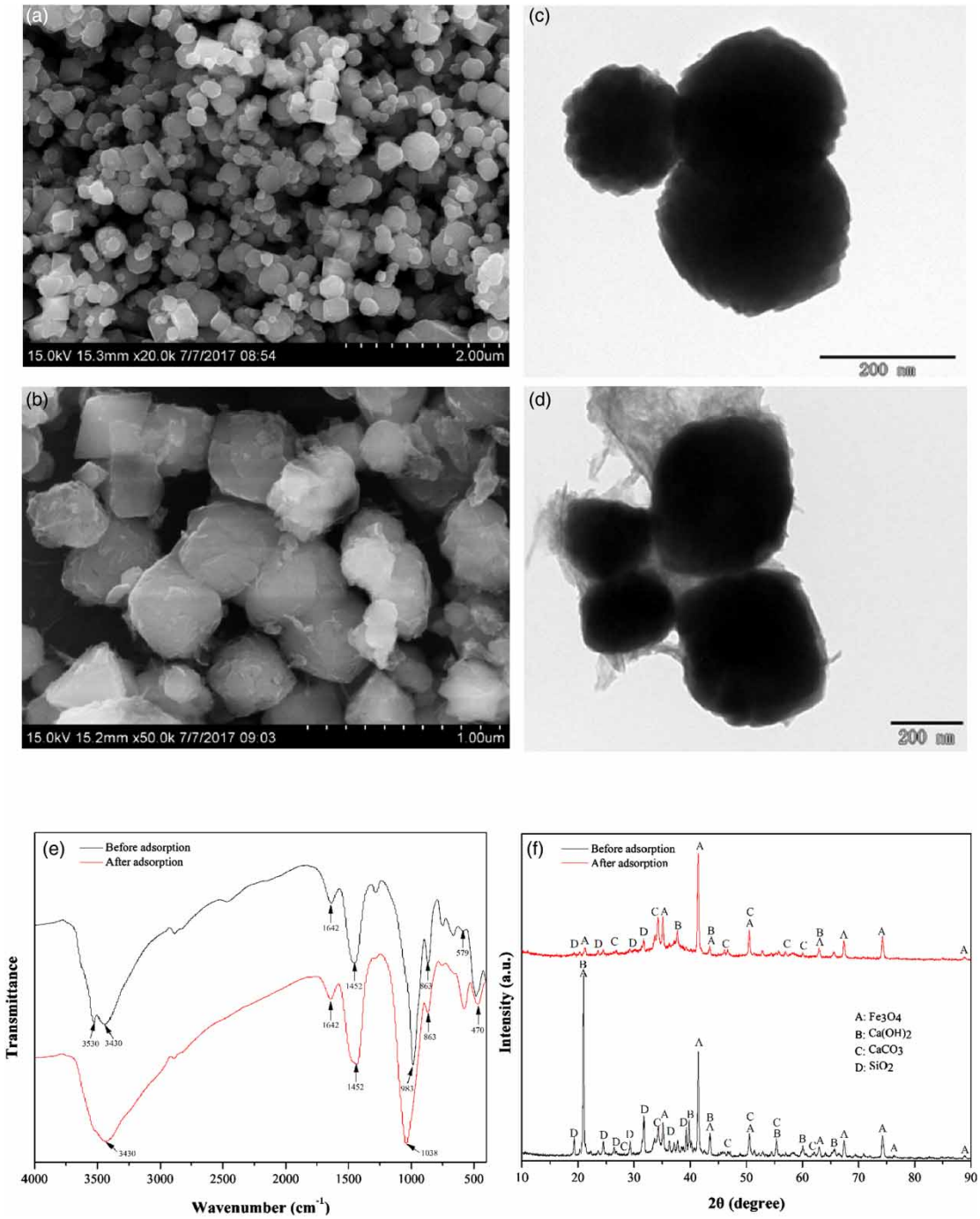

Figure 1 | The characterization of the synthesized Fe_3O_4 and Fe_3O_4@CSH: SEM image (a) and (b); TEM image (scale bar: 200 nm) (c) and (d); FTIR spectra of Fe_3O_4@CSH before and after phosphate adsorption (e); Fe_3O_4@CSH before and after phosphate adsorption (f).

The zeta potential of Fe_3O_4@CSH before and after phosphate adsorption was measured to determine the surface charge state of the adsorbent. The zeta potential data as a function of the pH of MNPs are shown on a zeta potential curve in Figure 3(a). The zeta potential values of Fe_3O_4@CSH showed a significant decrease over the whole pH range after phosphate adsorption. The zero charge (pH_{PZC}) of Fe_3O_4@CSH was 5.82 (Figure 3(a)), higher than that of the pH 5.35 solution. Therefore, this adsorbent acts as a positive charge and attracts the negatively charged phosphate ($H_2PO_4^-$, HPO_4^{2-}) electrostatically. The pH_{PZC} of P laden Fe_3O_4@CSH decreased from 3.92 to 2.82 with

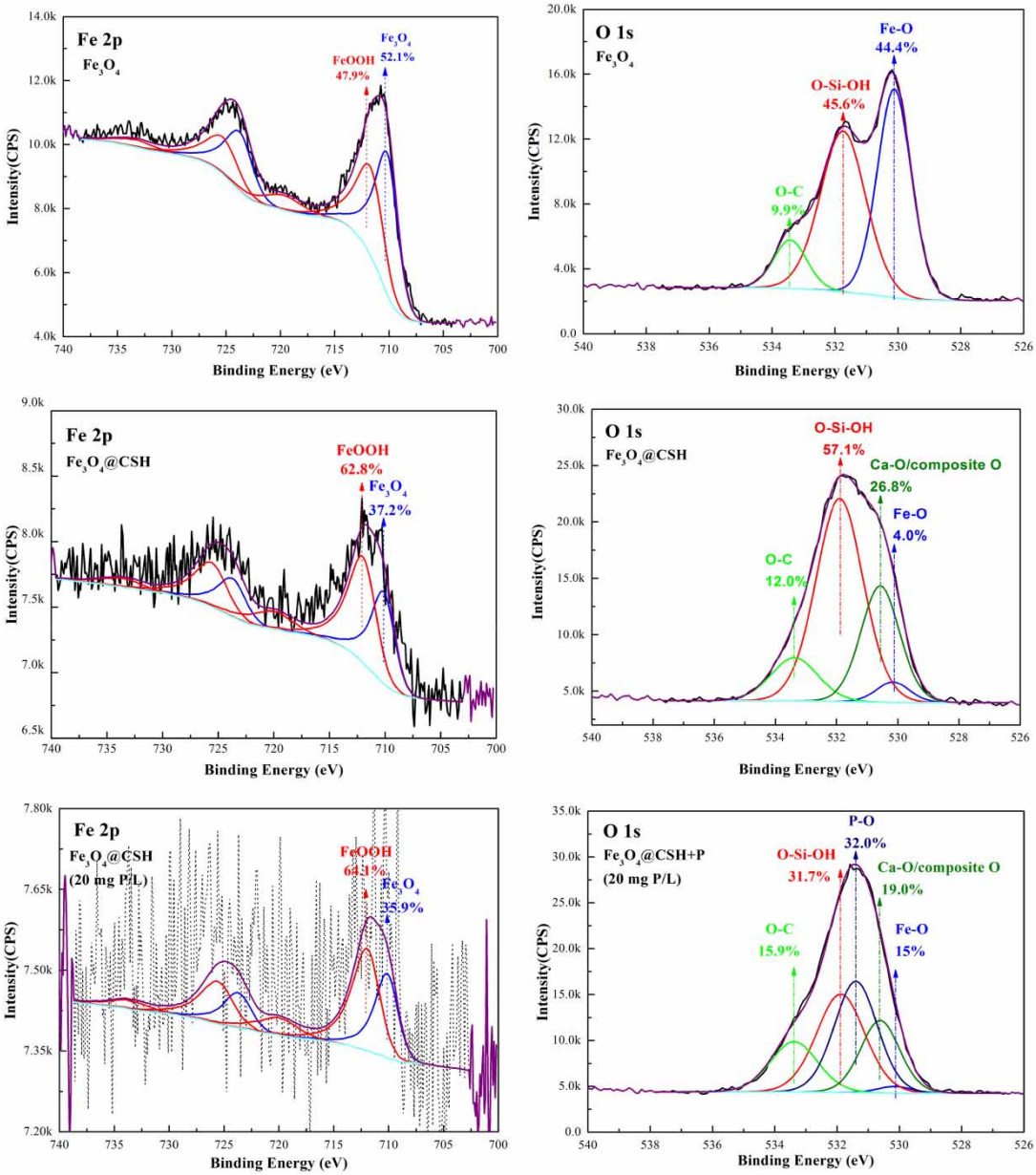

Figure 2 | The O 1 s and Fe 2p XPS spectra of Fe_3O_4, Fe_3O_4@CSH before and after the adsorption of phosphate.

Table 1 | Atomic content of elements in Fe_3O_4, Fe_3O_4@CSH particles before and after phosphate adsorption

	Atomic content (%)					
	Fe	O	C	Si	Ca	P
Fe_3O_4	8.84	34.9	56.26	–	–	–
Fe_3O_4@CSH	1.52	41.88	38.71	8.02	9.87	–
Fe_3O_4@CSH + P (20 mg P/L)	0.85	40.65	41.14	2.59	10.01	4.76

increasing initial P concentration, indicating that chemical adsorption of phosphate leads to a more negatively charged surface. Similar results have also been found for the chemical adsorption of phosphate on ZrO_2@Fe_3O_4 and Al_2O_3 (Nero *et al.* 2010; Fang *et al.* 2017).

The VSM for Fe_3O_4 and Fe_3O_4@CSH MNPs was measured; the saturated magnetization data are shown in Figure 3(b). The bare Fe_3O_4 and Fe_3O_4 after coating have saturated magnetization values of 82.66 emu/g and 15.42 emu/g, respectively, indicating a sharp decrease in

Table 2 | The Lorentzian peak shape fitting parameters for O 1 s XPS peak of Fe_3O_4, Fe_3O_4@CSH particles before and after phosphate adsorption

Sample	Peak	Position (eV)	Area	FWHM (eV)	Relative percent (%)
Fe_3O_4	Fe-O	530.1	17,796.2	1.276	44.4
	O-Si-OH	531.7	18,261.0	1.697	45.6
	O-C	533.4	3,981.4	1.226	9.9
Fe_3O_4@CSH	Fe-O	530.2	2,511.3	1.280	4.0
	Ca-O or composite O	530.6	16,626.0	1.490	26.8
	O-Si-OH	531.9	35,351.5	1.810	57.1
	O-C	533.4	7,456.3	1.800	12.0
Fe_3O_4@CSH + P (20 mg P/L)	Fe-O	530.2	1,000.0	1.280	1.5
	Ca-O or composite O	530.6	12,650.5	1.480	19.0
	P-O	531.4	21,326.6	1.620	32.0
	O-Si-OH	531.9	21,136.2	1.820	31.7
	O-C	533.4	10,578.9	1.780	15.9

magnetization (Figure 3(b)). This phenomenon results from the presence of silica and calcium layers that can attenuate the magnetization of Fe_3O_4, alongside the decrease in the magnetite fraction (Zhao *et al.* 2014). Despite this decrease in the saturation magnetization, magnetic separation can be realized within 1 min by dispersing particles in solution and then placing a magnet close to the glass bottle.

Adsorption kinetics, isotherm, and thermodynamic analyses

Adsorption kinetics

High P adsorption rates are desirable for economically viable phosphate removal and recovery from wastewater. Fe_3O_4@CSH materials were employed to adsorb phosphate from 20 mg P/L synthetic P solution at 25 °C, 35 °C, and 45 °C over a range of time periods. As shown in Figure 4, the kinetics in all cases showed a sharp initial slope in the first 1 h by comparison with other references (Nero *et al.* 2010; Fang *et al.* 2017), indicating that adsorption equilibrium was reached in a short time. This short equilibrium time can be attributed to the superior physicochemical adsorption of phosphate and to specific surface properties (e.g. porosity) that contribute to accelerated phosphate adsorption. The rapid adsorption kinetics demonstrate that this material has good potential for practical application to adsorption of phosphate from wastewater.

Table 3 | The Lorentzian peak shape fitting parameters for Fe 2p XPS peak of Fe_3O_4, Fe_3O_4@CSH particles before and after phosphate adsorption

Sample	Peak	Name	Position (eV)	Area	FWHM (eV)	Relative percent (%)
Fe_3O_4	Fe_3O_4	Fe 2p3/2	710.2	10,994.9	2.30	52.1
		Fe 2p1/2	723.8	5,497.5	2.76	
	FeOOH	Fe 2p3/2	711.7	8,092.8	2.70	47.9
		Fe 2p1/2	725.3	4,046.4	3.24	
		Fe 2p3/2 sat.	719.7	2,023.2	4.05	
		Fe 2p1/2 sat.	733.3	1,011.6	4.05	
Fe_3O_4@CSH	Fe_3O_4	Fe 2p3/2	710.1	1,753	2.3	37.2
		Fe 2p1/2	723.7	876.5	2.76	
	FeOOH (Fe^{3+} composite with SiO_2, CSH)	Fe 2p3/2	712.0	2,364.4	2.7	62.8
		Fe 2p1/2	725.6	1,182.2	3.24	
		Fe 2p3/2 sat.	720.0	591.1	4.05	
		Fe 2p1/2 sat.	733.6	295.5	4.05	
Fe_3O_4@CSH + P (20 mg P/L)	Fe_3O_4	Fe 2p3/2	710.1	389.8	2.30	35.9
		Fe 2p1/2	723.7	194.9	2.76	
	FeOOH (Fe^{3+} composite with SiO_2, CSH)	Fe 2p3/2	712.0	555.5	2.70	64.1
		Fe 2p1/2	725.6	277.7	3.24	
		Fe 2p3/2 sat.	720.0	138.9	4.05	
		Fe 2p1/2 sat.	733.6	69.4	4.05	

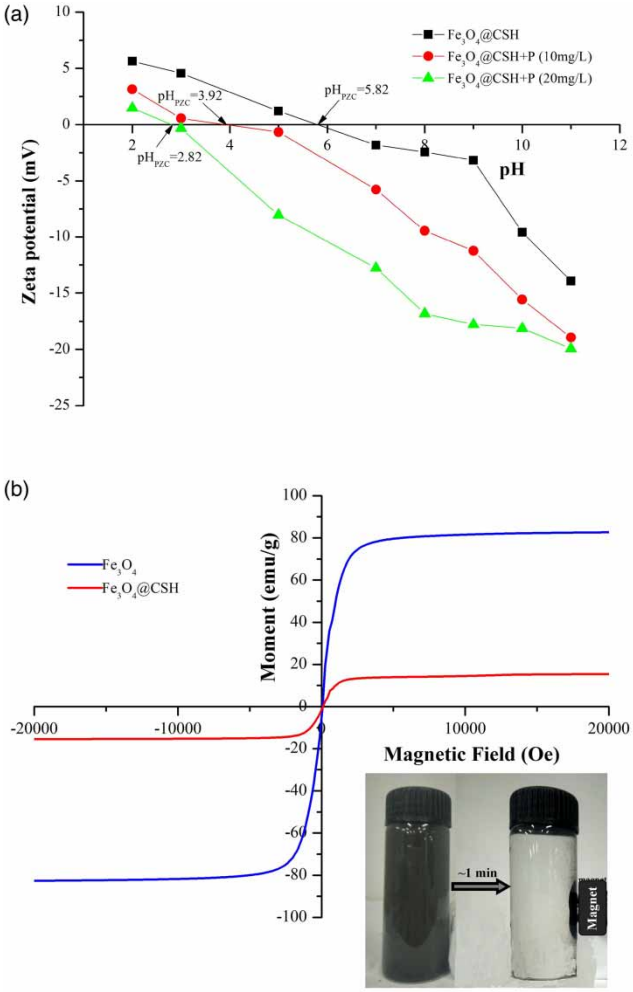

Figure 3 | Zeta potential of Fe_3O_4@CSH before and after the adsorption of phosphate (a); VSM of Fe_3O_4 and Fe_3O_4@CSH particles (the insert is aqueous solution with dispersed Fe_3O_4@CSH MNPs before and after magnetic separation using an external magnetic field) (b).

Kinetic parameters can be determined from the slope and intercept of a plot of t-q_t based on the application of Equations (5)–(7) to the experimental data in Table 4. As shown in Table 4, the correlation coefficients (R^2) indicate that the kinetic data fit the pseudo second-order model better than the pseudo first-order and Elovich models. A comparison of R^2 values indicates that phosphate adsorption on this material involved a chemisorption process. In addition, an increase in adsorption with increasing temperature was observed, indicating that a higher temperature results in considerably enhanced adsorption. Equilibrium experimental data were fitted to the pseudo second-order model. The calculated equilibrium adsorption capacities (q_e, mg P/g) were very close to the experimental equilibrium adsorption capacities (q_{exp}, mg P/g) as shown in Table 4.

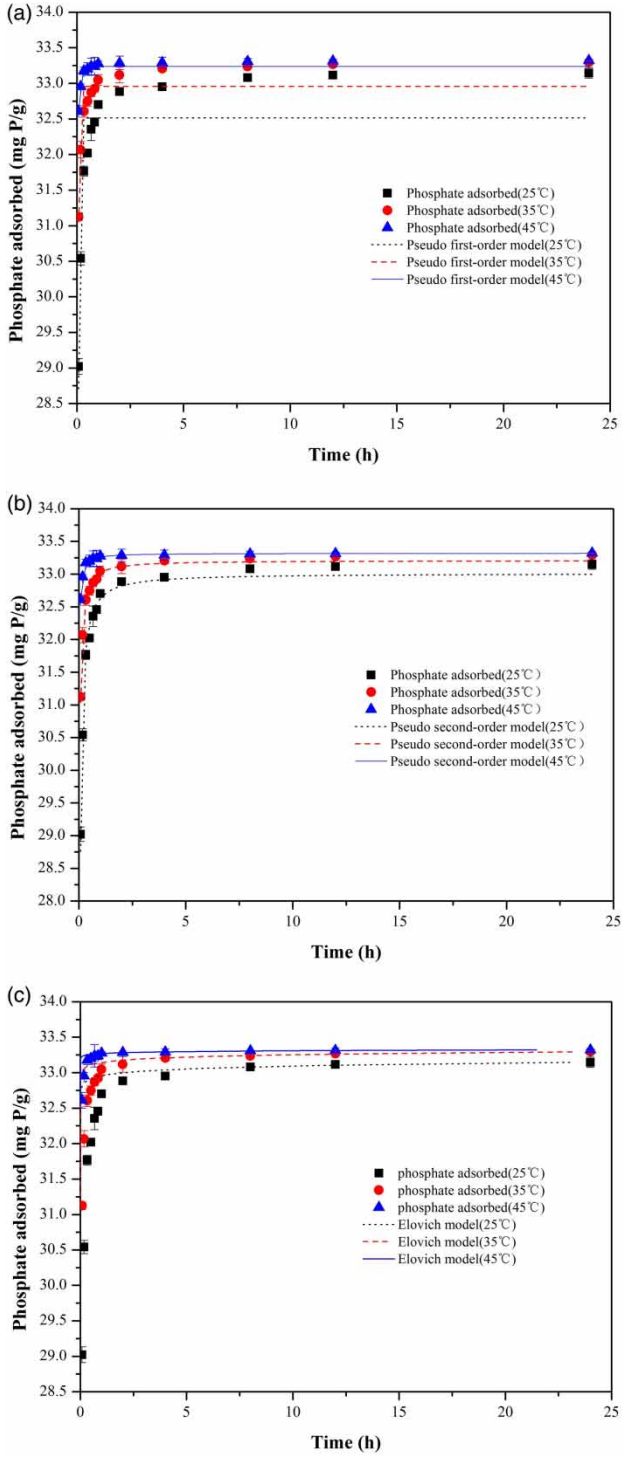

Figure 4 | Kinetic model: (a) the pseudo first-order model, (b) the pseudo second-order model and (c) Elovich kinetic model.

Adsorption isotherms

To further understand the phosphate adsorption mechanism and evaluate the efficiency of Fe_3O_4@CSH materials,

Table 4 | Kinetic model parameters obtained from model fitting to experimental kinetic data

	Pseudo first-order model			Pseudo second-order model				Elovich model		
Temperature (°C)	q_e (mg P/g)	k_1 (h^{-1})	R^2	q_e (mg P/g)	q_{exp} (mg P/g)	k_2 (h^{-1})	R^2	α (mg P g^{-1} h^{-1})	B (g mg P^{-1})	R^2
25	32.51	26.81	0.673	33.01	33.14	2.56	0.979	1.33×10^{244}	16.64	0.964
35	32.96	35.65	0.693	33.21	33.29	5.38	0.987	2.25×10^{301}	21.03	0.982
45	33.24	49.48	0.754	33.32	33.32	17.15	0.995	–	59.63	0.965

adsorption equilibrium was established and visualized using a plot of adsorbed P and residual P (C_e–q_e) in the solution. The initial P concentration was designed as a variable parameter to investigate the isotherms of phosphate adsorption onto these particles over 24 h. As shown in the adsorption isotherms (Figure 5(a)), Fe_3O_4@CSH materials exhibited a very strong adsorption affinity for phosphate, and it is clear that the modification with silica and calcium layers enhances the sorption capacity of MNPs considerably.

As shown in Figure 5(a), the isotherm exhibited a steep initial slope, suggesting that Fe_3O_4@CSH materials can act as effective adsorbents at relatively low P concentrations. From the correlation coefficients (R^2) and Chi-square (χ^2) analysis in Table 5, it appears that the Freundlich isotherm model was the best fit for describing the equilibrium isotherm data, implying that adsorbed phosphate forms a monolayer surface coverage on the Fe_3O_4@CSH and that chemisorption is the predominant adsorption mechanism. These results are consistent with the strong surface complexation between phosphate and OH functional groups; the possible reaction mechanisms are given in (1) and (2). The maximum adsorption capacity (Q_m) of the material obtained from the Freundlich isotherm model using Equation (13) was 55.84 mg P/g, higher than the magnetic adsorbents reported in previous literatures (Table 6).

Thermodynamic analyses

Calculated endothermic parameters are presented in Table 7. The negative values of ΔG^0 (−10.45 to −19.86 KJ/mol) calculated across the entire temperature range illustrate that adsorption of phosphate on these particles was spontaneous. Greater phosphate adsorption capacity was observed at higher temperatures, from 25 °C to 45 °C, as shown in Figure 5(b), indicating that the adsorption process was endothermic. Further, the order of phosphate adsorption on the Fe_3O_4@CSH in Figure 5(b) decreases as the phosphate adsorbed increases due to the Sorbent Concentration effect (Cs-effect) (Voice & Weber 1985). The diffusion rate of adsorbate molecules to the external layer of the adsorbents increased with increasing temperature because of the decrease in viscosity (Lyubchik *et al.* 2004). The positive value of ΔH^0 (129.84 KJ/mol) shown in Table 7 also indicates the endothermic nature of the adsorption processes. Therefore, higher temperatures are more favorable for phosphate adsorption. The positive value of ΔS^0 (470.76 J/K mol) indicates an increase in disorder at the solid–solution interface during the adsorption process; this disordered state is mostly due to the combination of phosphate with particle sites to form stable structures. The results demonstrate the strong affinity of the adsorbent to phosphate under optimized batch conditions.

Reusability of Fe_3O_4@CSH materials

The Fe_3O_4@CSH materials reuse improves the economic and environmental benefits of this material and increases its potential for practical application. The reusability of the material was therefore investigated over eight adsorption/desorption cycles using these particles in phosphate solution (20 mg P/L), and the results are shown in Figure 6. Fe_3O_4@CSH materials can maintain relatively high capacity over eight cycles (over 60%), although a slight reduction in phosphate adsorption occurred with increasing cycle number. After desorption, the adsorbed phosphate was concentrated in a caustic solution with a high P content. To recover P from this solution, calcium-containing chemicals (e.g., $CaCl_2$, $Ca(OH)_2$) should be added to the alkaline solution to convert the phosphate to calcium phosphate fertilizer for use in agriculture. This reusability indicates that, through a simple process, Fe_3O_4@CSH materials can act as potential adsorbents for practical environmental remediation and resource recovery.

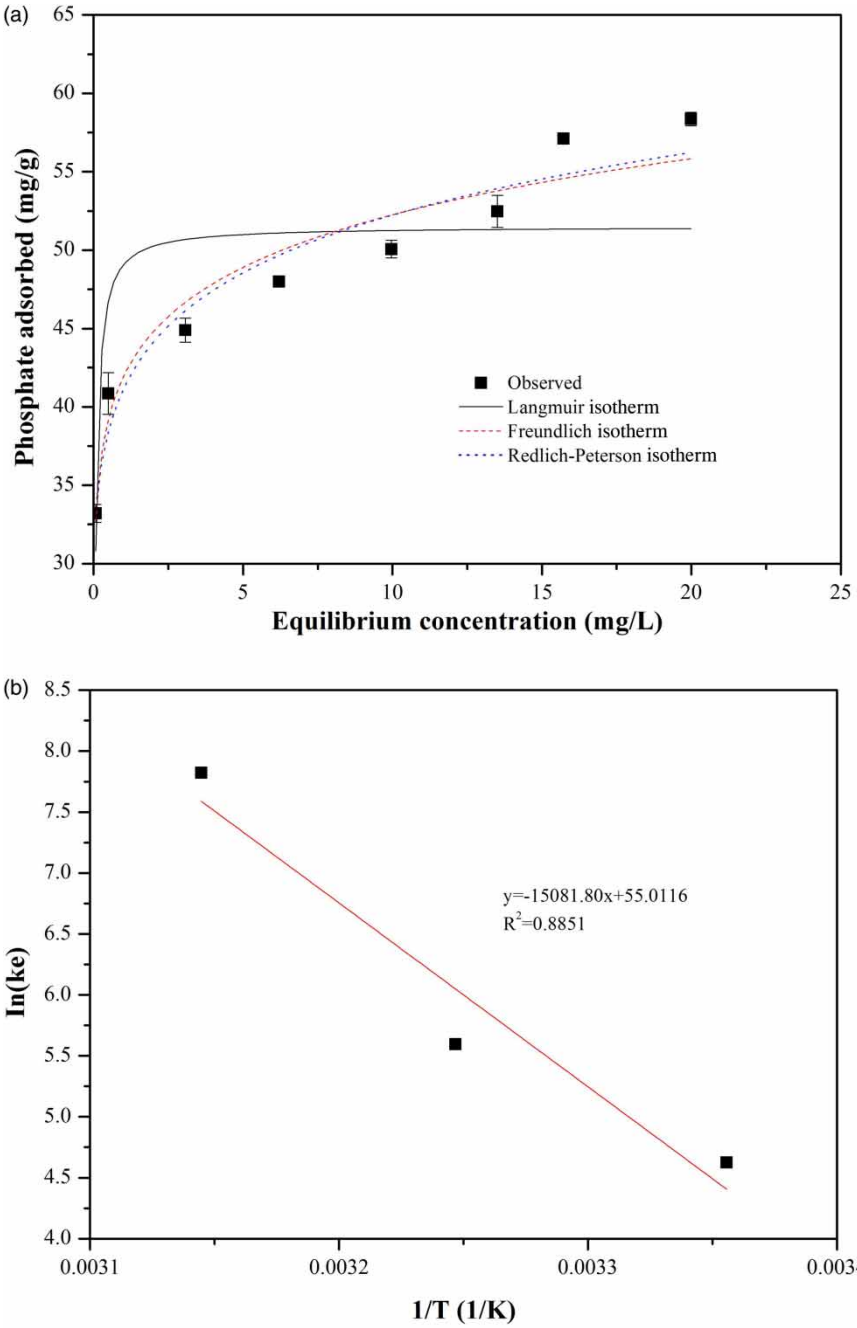

Figure 5 | Equilibrium isotherm model analyses with the Freundlich, Langmuir and Redlich-Peterson isotherm models (a); thermodynamic analysis for phosphate adsorption to Fe_3O_4@CSH materials (b).

Table 5 | Equilibrium isotherm model parameters obtained from model fitting to experimental kinetic data

Freundlich					Langmuir				Redlich-Peterson				
K_F (L/g)	1/n	Q_m (mg P/g)	R^2	χ^2	K_L (L P mg^{-1})	Q_{max} (mg P/g)	R^2	χ^2	K_R ((L/g)	K_R/a_R (L P mg-1)	g	R^2	χ^2
41.93	0.10	55.84	0.931	4.89	20.08	51.51	0.602	28.07	5.19×10^3	40.87	0.89	0.923	5.46

Table 6 | Comparison of phosphate adsorption capacity for Fe_3O_4 MNPs functioned with various functional groups

Materials	Sorption capacity (mg P/g)	Size (nm)	Reference
Fe_3O_4	20	20	Murphy & Riley (1962)
La (III)-modified Fe_3O_4@SiO_2	27.80	10–40	Song *et al.* (2006)
ZrO_2 @SiO_2@Fe_3O_4	6.33	About 400	Tang & Lo (2013)
ZrO_2 @Fe_3O_4	15.98	Over 200	Tang & Lo (2013)
Fe_3O_4@CSH	55.84	About 400	This work

Table 7 | Thermodynamic parameters for phosphate adsorption to Fe_3O_4@CSH materials

Temperature (°C)	ΔH° (KJ/mol)	ΔS° (J/K mol)	ΔG° (KJ/mol)
25	129.84	470.76	−10.45
35	–	–	−15.15
45	–	–	−19.86

CONCLUSION

In this study, an innovative magnetic calcium silicate composite material (Fe_3O_4@CSH) was synthesized and investigated for removal and recovery of phosphate from synthetic phosphate solution under optimized experimental conditions. Characterization of Fe_3O_4@CSH before and after phosphate adsorption by SEM, TEM, FTIR, XRD, XPS, zeta potential, and magnetic measurement indicated that phosphate adsorption was mainly dependent on chemisorption, and phosphate could be quickly separated by an external magnet. Based on observed experimental data, this research demonstrated that Fe_3O_4@CSH is effective for phosphate adsorption, with a maximum adsorption capacity of 55.84 mg P/g. The pseudo second-order model provided the best fit to the kinetic data and demonstrated that the adsorption of phosphate on Fe_3O_4@CSH occurred rapidly through chemical adsorption. The equilibrium data fitted well to the Freundlich isotherm model, implying dominant chemical adsorption by the formation of Ca-P precipitation, consistent with characterization results. Thermodynamic analysis suggested that phosphate adsorption to Fe_3O_4@CSH was a spontaneous and endothermic process. Additionally, Fe_3O_4@CSH was shown to be reusable over

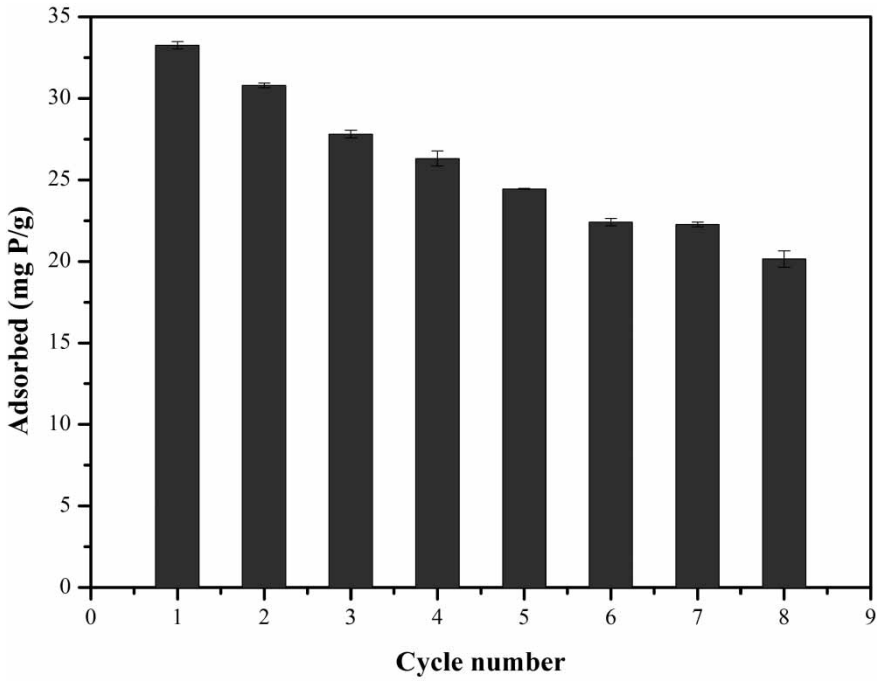

Figure 6 | Reusability of Fe_3O_4@CSH materials for phosphate recovery within eight cycles.

eight adsorption/desorption cycles. The results indicate that this material has great potential for phosphate recovery in practical applications.

ACKNOWLEDGEMENTS

This research was funded by the Major Science and Technology Project of Water Pollution Control and Management in China (2012ZX07101005), the National Science and Technology Support Program in China (2015BAL01B01), the Scientific Research Foundation of Graduate School of Southeast University (YBJJ1643), Natural Science Foundation of Jiangsu Province, China (BK20161146) and Water pollution control project in Taihu (TH2016203). We thank the anonymous reviewers for their constructive comments that improved the manuscript.

REFERENCES

Almatouq, A. & Babatunde, A. O. 2016 Concurrent phosphorus recovery and energy generation in mediator-less dual chamber microbial fuel cells: mechanisms and influencing factors. *Int. J. Environ. Res. Public Health* **13** (4), 375–387.

Correll, D. L. 1998 The role of phosphorus in the eutrophication of receiving waters: a review. *J. Environ. Qual.* **27** (2), 261–266.

Cordell, D., Drangert, J. O. & White, S. 2009 The story of phosphorus: global food security and food for thought. *Global Environ. Chang.* **19** (2), 292–305.

Dai, H., Lu, X., Peng, Y., Zou, H. & Shi, J. 2016 An efficient approach for phosphorus recovery from wastewater using series-coupled air-agitated crystallization reactors. *Chemosphere* **165**, 211–220.

Dai, H., Lu, X., Peng, Y., Yang, Z. & Zhsssu, H. 2017 Effects of supersaturation control strategies on hydroxyapatite (HAP) crystallization for phosphorus recovery from wastewater. *Environ. Sci. Pollut. R* **24** (6), 5791–5799.

Daou, T. J., Begin-Colin, S., Grenèche, J. M., Thomas, F., Derory, A., Bernhardt, P., Legar, P., Pourroy, G., Greneche, J. M. & Legaré, P. 2007 Phosphate adsorption properties of magnetite-based nanoparticles. *Chem. Mater.* **19** (18), 4494–4505.

Das, S., Pandey, A. K., Athawale, A. A. & Manchanda, V. K. 2009 Exchanges of uranium (VI) species in amidoxime-functionalized sorbents. *J. Phys. Chem. B* **113** (18), 6328–6335.

Drenkova-tuhtan, A., Mandel, K., Paulus, A., Paulus, K., Meyer, C., Hutter, F. & Gellermann, C. 2013 Phosphate recovery from wastewater using engineered superparamagnetic particles modified with layered double hydroxide ion exchangers. *Water Res.* **47** (15), 5670–5677.

Egle, L., Rechberger, H. & Zessner, M. 2015 Overview and description of technologies for recovering phosphorus from municipal wastewater. *Resour. Conserv. Recy.* **105**, 325–346.

Elzinga, E. J. & Sparks, D. L. 2007 Phosphate adsorption onto hematite: an in situ ATR-FTIR investigation of the effects of pH and loading level on the mode of phosphate surface complexation. *J. Colloid Interf. Sci.* **308** (1), 53–70.

Fang, L., Wu, B. & Lo, I. M. C. 2017 Fabrication of silica-free superparamagnetic ZrO_2@Fe_3O_4 with enhanced phosphate recovery from sewage: performance and adsorption mechanism. *Chem. Eng. J.* **319**, 258–267.

Foo, K. Y. & Hameed, B. H. 2010 Insights into the modeling of adsorption isotherm systems. *Chem. Eng. J.* **156** (1), 2–10.

Gilbert, N. 2009 The disappearing nutrient. *Nature* **461** (7265), 716–718.

Goswami, A. & Purkait, M. K. 2011 Kinetic and equilibrium study for the fluoride adsorption using Pyrophyllite. *Sep. Sci. Technol.* **46** (11), 1797–1807.

Guan, W., Ji, F., Chen, Q., Yan, P. & Zhang, Q. 2013 Preparation and phosphorus recovery performance of porous calcium-silicate-hydrate. *Ceram. Int.* **39** (2), 1385–1391.

Jordaan, E. M., Ackerman, J. & Cicek, N. 2010 Phosphorus removal from anaerobically digested swine wastewater through struvite precipitation. *Water Sci. Technol.* **61** (12), 3228–3234.

Li, H., Du, T., Xiao, H. & Zhang, Q. 2017 Crystallization of calcium silicate hydrates on the surface of nanomaterials. *J. Am. Ceram. Soc.* **100** (7), 3227–3238.

Loganathan, P., Vigneswaran, S., Kandasamy, J. & Bolan, N. S. 2014 Removal and recovery of phosphate from water using sorption. *Crit. Rev. Environ. Sci. Technol.* **44** (8), 847–907.

Luo, W., Hai, F. I., Price, W. E., Guo, W., Ngo, H. H., Yamamoto, K. & Nghiem, L. D. 2015 Phosphorus and water recovery by a novel osmotic membrane bioreactor-reverse osmosis system. *Bioresource Technol.* **200**, 297–304.

Lyubchik, S. I., Lyubchik, A. I., Galushko, O. L., Tikhonova, L. P., Vital, J., Fonseca, I. M. & Lyubchik, S. B. 2004 Kinetics and thermodynamics of the Cr (III) adsorption on the activated carbon from co-mingled wastes. *Colloids Surf. A* **242** (1), 151–158.

Mayer, B. K., Baker, L. A., Boyer, T. H., Drechsel, P., Gifford, M., Hanjra, M. A., Parameswaran, P., Stoltzfus, J., Westerhoff, P. & Rittmann, B. 2016 Total value of phosphorus recovery. *Environ. Sci. Technol.* **50** (13), 6606–6620.

Murphy, J. & Riley, J. P. 1962 A modified single solution method for the determination of phosphate in natural waters. *Anal. Chim. Acta* **27**, 31–36.

Nero, M. D., Galindo, C., Barillon, R., Halter, E. & Madé, B. 2010 Surface reactivity of α-Al_2O_3 and mechanisms of phosphate sorption: in situ ATR-FTIR spectroscopy and ζ potential studies. *J. Colloid Interface Sci.* **342** (2), 437–444.

Okano, K., Uemoto, M., Kagami, J., Miura, K., Aketo, T., Toda, M., Honda, K. & Ohtake, H. 2013 Novel technique for phosphorus recovery from aqueous solutions using amorphous calcium silicate hydrates (A-CSHs). *Water Res.* **47** (7), 2251–2259.

Renman, A. & Renman, G. 2010 Long-term phosphate removal by the calcium-silicate material Polonite in wastewater filtration systems. *Chemosphere* **79** (6), 659–664.

Sadeghi, S., Azhdari, H., Arabi, H. & Moghaddam, A. Z. 2012 Surface modified magnetic Fe_3O_4 nanoparticles as a selective sorbent for solid phase extraction of uranyl ions from water samples. *J. Hazard. Mater.* **215–216** (2), 208–216.

Sen, G. S. & Bhattacharyya, K. G. 2011 Kinetics of adsorption of metal ions on inorganic materials: a review. *Adv. Colloid Interface* **162**, 39–58.

Song, Y., Weidler, P. G., Berg, U., Nüesch, R. & Donnert, D. 2006 Calcite-seeded crystallization of calcium phosphate for phosphorus recovery. *Chemosphere* **63** (2), 236–243.

Song, W., Liu, M., Hu, R., Tan, X. & Li, J. 2014 Water-soluble polyacrylamide coated-Fe_3O_4 magnetic composites for high-efficient enrichment of U (VI) from radioactive wastewater. *Chem. Eng. J.* **246** (6), 268–276.

Tang, S. C. & Lo, I. M. 2013 Magnetic nanoparticles: essential factors for sustainable environmental applications. *Water Res.* **47** (8), 2613–2632.

Tarayre, C., De, C. L., Charlier, R., Michels, E., Meers, E., Camargo-Valero, M. & Delvigne, F. 2016 New perspectives for the design of sustainable bioprocesses for phosphorus recovery from waste. *Bioresource Technol.* **206**, 264–274.

Voice, T. C. & Weber, W. J. 1985 Sorbent concentration effects in liquid/solid partitioning. *Environ. Sci. Technol.* **19**, 789.

Wang, P., Wang, X., Yu, S., Zou, Y., Wang, J., Chen, Z., Alharbi, N. S., Alsaedi, A., Hayat, T. & Chen, Y. 2016 Silica coated Fe_3O_4 magnetic nanospheres for high removal of organic pollutants from wastewater. *Chem. Eng. J.* **306**, 280–288.

Yoon, S. Y., Lee, C. G., Park, J. A., Kim, J. H., Kim, S. B., Lee, S. H. & Choi, J. W. 2014 Kinetic, equilibrium and thermodynamic studies for phosphate adsorption to magnetic iron oxide nanoparticles. *Chem. Eng. J.* **236** (2), 341–347.

Zhang, J., Zhai, S., Shi, L., Xiao, Z., Song, Y., An, Q. & Tian, G. 2013 Pb (II) removal of Fe_3O_4@SiO_2-NH_2, core-shell nanomaterials prepared via a controllable sol-gel process. *Chem. Eng. J.* **215–216** (1), 461–471.

Zhao, Y., Li, J., Zhao, L., Zhang, S., Huang, Y., Wu, X. & Wang, X. 2014 Synthesis of amidoxime-functionalized Fe_3O_4@SiO_2 core-shell magnetic microspheres for highly efficient sorption of U (VI). *Chem. Eng. J.* **235**, 275–283.

Zong, P. F., Wang, S. F., Zhao, Y. L., Wang, H., Pan, H. & He, C. H. 2013 Synthesis and application of magnetic graphene/iron oxides composite for the removal of U (VI) from aqueous solutions. *Chem. Eng. J.* **220** (11), 45–52.

First received 22 October 2017; accepted in revised form 10 April 2018. Available online 18 April 2018